

1 Deep and rapid thermo-mechanical erosion by a  
2 small-volume lava flow

3 Gallant, E.<sup>1</sup> (egallant@mail.usf.edu), Deng, F.<sup>1</sup>, Connor, C.<sup>1</sup>,  
Dixon, T.H.<sup>1</sup>, Xie, S.<sup>1</sup>, Saballos, J.A.<sup>2</sup>, Gutiérrez, C.<sup>2</sup>,  
Myhre, D.<sup>3</sup>, Connor, L.<sup>1</sup>, Zayac, J.<sup>4</sup>, LaFemina, P.<sup>5</sup>, Charbonnier,  
S.<sup>1</sup>, Richardson, J.<sup>6,7</sup>, Malservisi, R.<sup>1</sup>, and Thompson, G.<sup>1</sup>

1: University of South Florida, School of Geosciences

2: Instituto Nicaragüense de Estudios Territoriales

3: University of South Florida, College of Marine Science

4: Earth and Environmental Sciences Program, The Graduate Center,  
City University of New York

5: Pennsylvania State University, Department of Geosciences

6: NASA Goddard Space Flight Center

7: University of Maryland, Department of Astronomy

4 May 4, 2020

5 **Abstract**

6 We document remarkably efficient thermo-mechanical erosion by a small-  
7 volume lava flow. Downcutting by a basaltic-andesite lava flow on the  
8 steep-sided Momotombo volcano, Nicaragua, occurred at 100 times the  
9 rate commonly reported for thermal erosion in lava flow fields, even though  
10 this flow was small-volume ( $0.02 \text{ km}^3$ ) and effused at a low rate for <1  
11 week. The lava flow incised into the pyroclastic substrate up to 30 m,  
12 with erosion depth controlled primarily by thermal reduction of substrate  
13 hardness. We show that incision depth decreases, approximately expo-  
14 nentially, with distance along the flow path, until erosion stopped and the  
15 flow became constructional. This transition occurs 650 m from the vent on  
16 a slope averaging a  $32^\circ$  incline. Results indicate that syn-eruptive erosion  
17 is an important morphological process on some steep-sided volcanoes that  
18 are predominantly composed of layered pyroclasts. Rapid erosion and  
19 incision increased flow run-out for the 1905 flow, which in turn directed  
20 the flow and run-out of the 2015 lava flow. Mapping and understanding  
21 these features is critical for improving lava flow hazard assessments and  
22 provides insight into the construction and growth of composite cones.

23  
24 *Non-peer reviewed preprint submitted to EarthArXiv and Elsevier. This*  
25 *paper has been accepted and published in EPSL.*

## 26 **1 Introduction**

27 Lava flows are responsible for altering landscapes on geologically short timescales.  
28 The overwhelming majority of lava flows construct topography by building  
29 raised channels and/or compound flow fields, both of which evolve through  
30 time and along-flow (Kerr et al., 2006; Dietterich and Cashman, 2014). The  
31 morphologies of flow features are mainly determined by the composition and ef-  
32 fusion rate of the flow, as well as the pre-existing and syn-eruptive topography  
33 (Richardson and Karlstrom, 2019; Bilotta et al., 2019). These factors also con-  
34 trol the thickness of lava flows, which in turn influence a flow’s run-out distance  
35 and inundation hazard potential (Kilburn and Lopes, 1988; Dietterich et al.,  
36 2017). A small fraction of channelized flows and lava tubes erode into older  
37 surfaces during emplacement via thermal, mechanical, or thermo-mechanical  
38 processes (Greeley et al., 1998; Fagents and Greeley, 2001; Kerr, 2001; Siewert  
39 and Ferlito, 2008; Hurwitz et al., 2010, 2013).

40 The 1905 eruption of Momotombo volcano, Nicaragua, provides an exam-  
41 ple of thermo-mechanical erosion by a small volume ( $<0.02 \text{ km}^3$ ) lava flow on  
42 a steep-sided edifice (Figs. 1 and 2). We first document the morphology of  
43 the channel using a combination of satellite and terrestrial radar generated dig-  
44 ital elevation models (DEMs) from 2012–2017. Erosion depths from the 1905  
45 flow are then calculated by reconstructing pre-channel topography, extracting  
46 cross-sectional profiles, and calculating the maximum difference between the  
47 measured and modeled surfaces normal to the channel. We use these results  
48 to test thermal and thermo-mechanical models of erosion. Model inputs are in-  
49 formed by observations from Momotombo’s most recent eruption in 2015, which  
50 we capture with a range of satellite and ground-based observations. We find the  
51 channel was thermo-mechanically eroded by a lava flow that erupted in 1905.  
52 Additionally, we assert that thermo-mechanical erosion is an important mor-

53 phological process on some steep-sided volcanoes composed predominantly of  
54 layered pyroclasts. This study is the first to look at lava flow erosion on steep  
55 sided slopes, expands our knowledge of the rate at which syn-eruptive erosion  
56 occurs, and mathematically couples thermal and mechanical models of erosion.

## 57 **2 Background**

### 58 **2.1 Erosion by Lavas**

59 Erosion by lava has been hypothesized for the formation of rilles on both Mars  
60 (Carr, 1974; Dundas and Keszthelyi, 2014) and the Moon (Hulme, 1973; Head  
61 and Wilson, 2017; Wilson and Head, 2017), canali on Venus (Baker et al., 1992;  
62 Williams-Jones et al., 1998), and channels on Io (Schenk and Williams, 2004).  
63 Studies of active erosion by flowing lava have occurred on the island of Hawai'i  
64 during the 1972–1974 Mauna Ulu eruption and the initial stages of the 1983-2018  
65 Pu'u O'o eruption, where erosion rates of 4 cm depth/day and 10 cm depth/day  
66 were observed in lava tubes via skylights, respectively (Peterson et al., 1994;  
67 Kauahikaua et al., 1998). Erosion by turbulent komattite flows during the  
68 Archean, responsible for large Ni-sulphide ore deposits, is also widely noted  
69 (Williams et al., 1998; Beresford et al., 2002; Staude et al., 2017).

#### 70 **Thermal Erosion**

71 Thermal erosion occurs when lava moves with sufficient flux and temperature to  
72 melt and incise the underlying terrain (Kerr, 2001). Thermal erosion by flowing  
73 lava requires the complete or partial melting and assimilation of a substrate  
74 into the overriding flow. A lava flow's total available thermal energy ( $E_{thermal}$ ),  
75 sourced from advection and crystallization, is modeled as:

$$E_{thermal} = m_l[c_{pl}(T_l - T_s) + \phi F] \quad (1)$$

76 where  $m_l$  is the mass of the erupted lava,  $c_{pl}$  is the specific heat capacity of  
77 the lava,  $T_l$  is the erupted temperature of the lava,  $T_s$  is the initial temperature  
78 of the environment into which heat is being transferred (the substrate in this  
79 case),  $\phi$  is the mass fraction crystallization, and  $F$  is the latent heat of fusion  
80 (Wooster et al., 1997). Lava flows are an open system where available thermal  
81 energy is eventually balanced out by heat loss through conduction, convection,  
82 and radiative heat transfer. Studies of the thermal energy balance of lava flows  
83 on Mt Etna show that upwards of 85% of energy was retained during the initial  
84 phases of the eruption, which can be used to further bound the amount of energy  
85 available to melt and erode the substrate (Wooster et al., 1997; Patrick et al.,  
86 2004). The presence of multiple heat sinks also highlights the fact that not all  
87 available thermal energy can be partitioned into eroding the substrate, so we  
88 need to quantify heat transfer between the base of the lava flow and substrate.  
89 The rate of conductive heat transfer into the substrate (i.e., the growth of a  
90 thermal boundary layer) can be modeled as:

$$\frac{dy}{dt} = \frac{\eta_T \sqrt{\kappa}}{t} \quad (2)$$

91 where  $y$  is the depth into the substrate,  $t$  is the duration of the flow,  $\eta_T$  is a di-  
92 mensionless similarity variable, and  $\kappa$  is the thermal diffusivity (Turcotte et al.,  
93 2002; Fagents and Greeley, 2001). Thermal diffusivity is based on the relation-  
94 ship between thermal conductivity ( $k$ ), substrate density ( $\rho_s$ ), and specific heat  
95 of the substrate ( $c_{ps}$ ), shown as:

$$\kappa = \frac{k}{\rho_s c_{ps}} \quad (3)$$

96 The dimensionless similarity variable,  $\eta_T$ , is related to the complementary error  
97 function (*erfc*) and a dimensionless temperature ratio ( $\theta_r$ ),

$$\eta_T = \text{erfc}^{-1}\theta_r \quad (4)$$

98 The dimensionless temperature ratio,  $\theta_r$ , is a measure of the relationships be-  
99 tween the temperature at the onset of thermo-mechanical erosion of the sub-  
100 strate,  $T_e$  and the temperature of the lava,  $T_l$ , shown as:

$$\theta_r = \frac{T_e - T_s}{T_l - T_s} \quad (5)$$

101 The growth of this boundary layer, which controls the rate of thermal erosion  
102 into the substrate, is illustrated in Figure 3 and described in Equation 2.

### 103 **Mechanical Erosion**

104 Mechanical erosion occurs when the wearing material (the lava flow) is harder  
105 than the substrate (the edifice) (Sklar and Dietrich, 1998; Siewert and Ferlito,  
106 2008; Hurwitz et al., 2010). This relationship is captured by the wear coefficient,  
107  $k$ , determined by the relationship between the wear volume, the sliding distance  
108 of the flow, the normal load, and the hardness of the wearing material. For  
109 similar material on Mt Etna, a range of  $10^{-2}$ - $10^{-3}$  for  $k$  has been calculated  
110 (Siewert and Ferlito, 2008). For context, a range of  $k \sim 10^{-1}$ - $10^{-5}$  characterize  
111 abrasive and erosive wear (Zum Gahr, 1998). The early stages of an eruption  
112 are most conducive to erosion because flow velocity is often highest and basal  
113 friction is also high because of the vertical load (Siewert and Ferlito, 2008;  
114 Hurwitz et al., 2010). Mechanical erosion as a function of substrate hardness  
115 can be modeled as:

$$H = \frac{k\rho ghvts\sin\theta}{d_{channel}} \quad (6)$$

116 where  $H$  is the hardness of the substrate,  $\rho$  is the density of the lava flow,  $h$  is  
 117 the thickness of the lava flow,  $v$  is the velocity of the lava flow,  $\theta$  is the slope of  
 118 the edifice, and  $d_{channel}$  is the depth of erosion. This equation implies that the  
 119 depth of an eroded channel will be constant, so long as the velocity of the flow  
 120 is constant. If the depth of the channel changes with distance, then either the  
 121 velocity of the flow is changing, or the hardness,  $H$ , is changing, or both. Given  
 122 that velocity changes in lava flows are readily observed and erosion appears to  
 123 be a rarer phenomena, it's likely that a change in hardness is the driving factor  
 124 for this process. Hardness, the ability of a material to resist deformation, is  
 125 equivalent to approximately one-third of the tensile strength of the material (the  
 126 yield strength). The yield strength is an exponential function of temperature,  
 127 which means that  $H$  can also be modeled as a function of temperature:

$$H \approx \frac{ae^{(-bT_i - e)}}{3} \quad (7)$$

128 where  $a$  and  $b$  are flow-dependent variables that vary with magma composition  
 129 and  $e$  is Euler's number. This relationship describes softening of the substrate as  
 130 its temperature, starting at  $T_i$  and ending at  $T_e$ , increases over time. This means  
 131 that mechanical lava erosion models presented in Siewert and Ferlito (2008) can  
 132 be reworked to become thermo-mechanical models. We note that experimental  
 133 data have indicated that the Arrhenius relationships shown in Equation 7 break  
 134 down around the glass transition point (Miller, 1963; Gottsmann and Dingwell,  
 135 2002).

## 136 **2.2 Geology of Momotombo and Recent Activity**

137 Momotombo (1,297 m) is located at the southern end of the Cordillera de Los  
138 Maribios in central Nicaragua (Fig. 1). The edifice is composed primarily of  
139 basaltic to basaltic andesite lavas, cinders, and other tephra that erupted dur-  
140 ing the last 4,500 years (Kirainov et al., 1988). Sixteen historical eruptions  
141 have been documented, the majority of which have been strombolian to vio-  
142 lent strombolian (Volcanic Explosivity Index (VEI) 1-2), with several plinian  
143 events (up to VEI 4) (Global Volcanism Program, 2017). A VEI 4 eruption  
144 in 1605-1606 and large earthquake in 1610 led to the abandonment of city of  
145 León (Viejo), the capitol of the region at that time (Sapper, 1925). Though the  
146 specific morphological changes to the edifice from the 1605-1606 plinian event  
147 are not well documented, it's possible that serious damage to the structural in-  
148 tegrity of the summit occurred given the impact on surrounding municipalities  
149 (Sapper, 1925). The subsequent steady activity throughout the 1800's rebuilt  
150 the summit from cinders, agglutinate, and channelized lava flows, as shown in  
151 photographs from the late 1800's and early 1900's (Vincent, 1890; Interconti-  
152 nental Railway Commission, 1898; Sapper, 1925). Ngauruhoe (New Zealand)  
153 (Hobden et al., 2002), Izalco (El Salvador) (Carr and Pontier, 1981), and Cerro  
154 Negro (Nicaragua) (Hill et al., 1998; Courtland et al., 2012) have built moder-  
155 ately sized pyroclastic cones in only a few hundred years and can provide further  
156 insight into rapid rates of edifice construction.

157 The 1905 eruption (VEI 2) occurred between January 16-21 (Sapper, 1925).  
158 The basaltic andesite lava flow was accompanied by an eruptive column of suf-  
159 ficient height to deposit ash 15 km to the west on the city of León. The effusive  
160 component consisted of an eruptive volume of  $<0.02 \text{ km}^3$  of basaltic andesite  
161 (Fig. 1). Intermittent explosions occurred that sent incandescent blocks and  
162 bombs "a great distance" from the crater (Sapper, 1925). First person accounts

163 also describe destruction to the summit during the eruption, which may have  
164 resulted in the drainage of a small summit lava lake (Sapper, 1925) (Fig. 2).  
165 The 1905 eruption was followed by 110 years of quiescence, which ended on 30  
166 November, 2015. A small volume basaltic andesite lava flow was emplaced be-  
167 tween 1 December and 7 December, 2015, and was followed by several months  
168 of intermittent explosions (Global Volcanism Program, 2017).

## 169 **3 Methods and Results**

### 170 **3.1 Digital Elevation Model Generation**

#### 171 **3.1.1 TanDEM-X Satellites**

172 Digital elevation models (DEMs) were generated from TanDEM-X Satellites  
173 (TDX) and collected on 24 October, 2012 and 18 March, 2017. These DEMs,  
174 which also capture the change in topography because of the eruption in 2015–  
175 2016, allow us to obtain baseline measurements for the 1905 channel (Fig. 4)  
176 and determine if any erosion occurred during the most recent eruption. The  
177 bistatic mode of TDX allows these two satellites to fly in tandem formation and  
178 observe the same ground point simultaneously (Krieger et al., 2007). We note  
179 that the flight paths for these acquisitions were not the same, which resulted in  
180 an offset because of a heading difference of  $\sim 21^\circ$ .

181 GAMMA software (Werner et al., 2000) was used to process the TDX SAR  
182 images to generate DEMs with the InSAR (Interferometric Synthetic Aperture  
183 Radar) technique (e.g., Deng et al., 2019). A 30-m SRTM (Shuttle Radar Topog-  
184 raphy Mission) DEM provided independent ground control points. Two (range)  
185 by two (azimuth) pixel multilooking was used to reduce speckle noise. The final  
186 DEMs have a spatial resolution of  $5 \times 5$  meters with a vertical precision of  
187  $< 2$  m.



### 188 **3.1.2 Terrestrial Radar**

189 We employed terrestrial radar interferometry (TRI) to assess the level of noise  
190 in our topographic profiles (described below) from the 2017 TDX acquisition.  
191 Although this comparison does not give us a direct assessment of noise for the  
192 2012 DEM (the model from which we are measuring channel incision depths),  
193 it allows direct comparison with the 2017 TDX data. TRI is a ground-based  
194 scanning radar that measures the amplitude and phase of a backscattered mi-  
195 crowave signal. A GAMMA real aperture radar operating at Ku-band (1.74 cm  
196 wavelength) was used for this study. The TRI has one transmitting antenna  
197 and two receiving antennas, which allows for topographic mapping with a single  
198 scan (e.g. Dixon et al., 2012; Caduff et al., 2015; Voytenko et al., 2015; Xie  
199 et al., 2018; Deng et al., 2019). The resolution of the range measurements is  
200  $\sim 1$  m, and the azimuth resolution varies linearly with distance (e.g., 1.8 m at  
201 1 km distance, 7 m at 4 km). The spatial coverage of TRI is smaller than the  
202 satellite data, but covers most of the region of interest for this study. Details  
203 of TRI data processing for DEM generation are given in Strozzi et al. (2012)  
204 and Xie et al. (2018). TRI surveys were conducted in December 2015 and April  
205 2016. We use results from the 2016 campaign because it occurred towards the  
206 end of the eruption period and is temporally closer to the 2017 TDX acquisition.  
207 The TRI DEM has a  $5 \times 5$  m resolution with an accuracy  $< 5$  m and covers the  
208 incised portion of the channel (Fig. S1).

### 209 **3.2 Channel Profiles and Depth Calculation**

210 Previous GIS-based methods used to determine paleotopography of volcanic  
211 terrains (e.g., Germa et al., 2015) interpolate missing topography by connecting  
212 high points in elevation. Studies of fluvial channel erosion in steep terrain  
213 generally do not deal with incision into conical edifices (Robl et al., 2008; Fox,

214 2019). Additionally, these approaches model down-section and not cross-section  
215 morphology, which we require to accurately measure incision depth and extract  
216 cross-section profiles. We developed an elliptical least-square best-fit contour  
217 method to obtain incision depths along the channel on Momotombo’s steep  
218 slopes to fill this application gap. We use this method to obtain channel depths  
219 and cross-channel profiles from the 2012 and 2017 TDX DEMs and the 2016  
220 TRI DEM. Our depth measurements are minimum values, as it is likely that  
221 the eroding flow would have emplaced some volume of lava within the channel.  
222 We also use this method to determine if any incision occurred during the 2015  
223 lava flow. Additionally, comparing the post-2015 TDX and TRI DEMs provides  
224 an indication of noise within our channel measurements.

225 This approach measures incision depth against modeled paleotopography  
226 created from optimized elliptical contours. A path down the channel’s center  
227 was defined with a sampling density set to the resolution of the DEM (5 m  
228 for this study)(Fig. S2a). The widths of the channel and levees, determined  
229 visually, were masked out in order to separate their signal from the overall signal  
230 of the cone. A refined elliptical fit for the uppermost contour of the channel path  
231 was calculated by minimizing the mean-squared difference between the actual  
232 elevation contour and an elliptical contour. This optimized ellipse was then used  
233 to calculate a fit to the elevation contour below. This second recalculated ellipse  
234 was then fit to the next elevation contour, and so forth, until the end of the  
235 designated channel path was reached. The output of this process is a modeled  
236 paleotopography with no channel or levee structures (Fig. S2b). The incision  
237 depth was calculated against the modeled paleotopography. The normal vector  
238 to the paleotopographic model was calculated at each point, spaced 5 m apart  
239 along each elliptical contour. As before, the normal vector was calculated by  
240 fitting a plane to 8 adjacent points (three from the contour above, three from

241 the contour below, and two adjacent points from the same contour) (Fig. S2c).  
242 The DEM was then re-orientated such that the z-axis was coincident with the  
243 calculated normal vector. The incision depth was returned as a weighted average  
244 of the constituent points, with weighting criteria based on the distance of the  
245 points to the center of the plane (i.e., the point closest to the center had the  
246 greatest weight) (Fig. S2d). This process was repeated for each point along the  
247 contour, and then for every contour. This process allowed us to measure the  
248 incision depth throughout the channel while removing the conic signal of the  
249 edifice (Fig. 5). Incision depth varied from 35 m at the summit rim and tapers  
250 off to 0 at  $\sim 600$  m elevation. We calculate the eroded volume of the channel  
251 to be  $4 \times 10^5 \text{ m}^3$ . A profile of each cross-channel contour was calculated for the  
252 2012 and 2017 TDX and 2016 TRI DEMs (Fig. 7).

253 Results show the pre-2015 eruption channel extended down the northeast  
254 side of the edifice from the summit and incised into the summit (Fig. 5). The  
255 2015 lava flow follows the same path as the pre-eruption channel (Fig 7). The  
256 elliptical contour fit method was also applied to the 2016 TRI DEM. Data gaps  
257 within the DEM were filled using a regularized spline with tension interpolation  
258 method in QGIS and the same process described above was utilized. We provide  
259 the code for this method (S1) and an additional code for a circular fit method  
260 in the Supplemental Documentation (S2).

## 261 4 Discussion

### 262 4.1 Channel Origins

263 The difference between modeled paleotopography and the 2012 TDX DEM  
264 shows that a channel has cut into the edifice. The distribution of lava flows  
265 beneath the 1905 units, shown in Figure 1, implies that no structure existed in

266 this location prior to 1905 to consistently direct the path of subsequent lava flows  
267 (as was the case for the 2015 eruption). No historical reports note a leveed lava  
268 channel on the NE flank of Momotombo prior to the 1905 eruption (Vincent,  
269 1890; Intercontinental Railway Commission, 1898; Sapper, 1925). Examination  
270 of the area surrounding Momotombo shows no down-slope deposition of suffi-  
271 cient volume to support a channel having carved into the NE edifice prior to the  
272 1905 eruption by environmental erosion (e.g. hydrologic erosion) and then in-  
273 filled by subsequent lava flows. The rest of the edifice is similarly devoid of any  
274 large-scale drainage features (e.g. barrancas, rilles, or gullies). DEM analyses  
275 show the channel width is uniform from summit to low on the slopes (Fig. 4).  
276 Incised channels on other volcanoes (e.g., Merapi, Nevado del Ruiz) are gener-  
277 ally much wider at the mouth, less consistent in width, and are less linear than  
278 Momotombo's channel because they are related to more violent hazards (e.g.,  
279 pyroclastic density currents and lahars). Results also show it was unlikely that  
280 erosion occurred during the 2015 lava flow, given that it flowed over the armored  
281 channel and not a variably consolidated slope of cinders and spatter/agglutinate  
282 (Fig. 7). In the absence of evidence that suggests otherwise, we conclude that  
283 channel most likely formed during the emplacement of the 1905 lava flow.

#### 284 **4.1.1 Thermal Erosion**

285 The total energy emitted by the 1905 lava flow, calculated using Equation 1,  
286 is about  $7 \times 10^{16}$  J for an eruptive volume of  $2 \times 10^7$  m<sup>3</sup>. Taking into account  
287 the energy balance between heat sources (85% retained) and sinks (15% lost)  
288 described in Wooster et al. (1997), we calculate that  $6 \times 10^{16}$  J is the minimum  
289 amount of the original energy that remained within the flow. Although the  
290 length of time used to calculate this ratio for the Mount Etna eruption was  
291 greater than the duration of the Momotombo eruption, it is helpful to place a  
292 first order constraint on how much thermal energy is lost into the environment.

293 We calculate the total energy needed to fully erode the channel is about 2  
294  $\times 10^{14}$  J, by substituting the mass of the eroded section of the channel into  
295 Equation 1. Although we find that sufficient energy exists within the system to  
296 erode the substrate, we note that not all of the energy present is available for this  
297 purpose. Had all of this energy been used to erode, the thermal loss would have  
298 been sufficiently great that the emplaced flow would be much thicker and shorter  
299 than what is observed. Modeling the depth of heat transfer into the substrate  
300 as a function of time using Equation 2 estimates the growth of the substrate  
301 thermal boundary layer at 8.8 cm per day when we account for the reduced  
302 density of cinders in our thermal diffusivity calculation ( $\sim 1000 \text{ kg m}^{-3}$  for our  
303 study area). Thermal erosion rates in Hawaiian tubes and channels can reach  
304  $\sim 10$  cm per day (Kauahikaua et al., 1998); given the lower temperature of lavas  
305 erupted on Momotombo, a slower rate of thermal boundary layer growth makes  
306 sense. Given the short duration of the 1905 eruption ( $< 1$  week; Sapper, 1925),  
307 thermal erosion by itself is unlikely to have formed the observed morphology.

#### 308 **4.1.2 Thermo-mechanical Erosion**

309 Conceptually, once the near-subsurface reaches the threshold temperature, which  
310 we assert is the glass transition ( $T_e$ , which is about 1013 K for basaltic rocks,  
311 Giordano et al., 2005), the hotter subsurface material begins to creep/flow and  
312 is transported downhill by the lava flow. This implies that the thermal bound-  
313 ary layer reaches some critical thickness and is then eroded away mechanically  
314 by the lava flow. While this process surely contributes to incision of the channel,  
315 it cannot fully account for the observed depths. It is possible  $H$  varies with dis-  
316 tance along the channel because the underlying substrate changes from very soft  
317 material at the top of the cone to harder material lower on the flanks. We reject  
318 this because the surface of the edifice is a relatively uniform slope without major  
319 lithologic changes. These results help us understand how the material hardness

320 of the substrate,  $H$ , is reduced over time as the lava flow moves downslope.  
321 Hardness is related to measurable mechanical properties (e.g., uniaxial com-  
322 pressive strength, shear/tensile strength, shear modulus). Siewert and Ferlito  
323 (2008) report  $H$  as being approximately 1/3 of the tensile strength of rock. As-  
324 suming this to be valid, and that tensile strength is approximately 1/10 of the  
325 compressive strength (e.g., Jaeger et al., 2007), then the value of  $H$  of the cinders  
326 ( $\sim 4 \times 10^6$  Pa) corresponds to compressive strength in the region of  $\sim 120$  MPa.  
327 For comparison, basaltic lavas can have compressive strengths of over 300 MPa  
328 (e.g., Farquharson et al., 2016).

329 We assume that the growth and removal of the thermal boundary layer over  
330 time can be approximated as a steady state process, captured by the depth of  
331 incision at each point along the channel. An exponential was fit to the incision  
332 depth data to extract the quadratic function of  $d_{channel}$  in terms of incision  
333 depth and elevation (Fig. 9). We solve for  $H$  and find that the transition from  
334 erosion to construction happens around  $4 \times 10^6$  Pa. Modeling the results in this  
335 way suggests that the hardness of the substrate increases as a function of time,  
336 but note that we use depth as proxy for time. Realistically, the deepest incision  
337 points are closest to the vent because they have been exposed to erosive work for  
338 a greater amount of time. The function modeled from Equation 6 tackles that  
339 problem from the opposite perspective (i.e., it models the decrease in erosive  
340 depth, which suggests increase in hardness). We know that temperature is  
341 increasing in the substrate based on the relationships described in Equation 2,  
342 which decreases the hardness, so we revise these results and report them as a  
343 decrease in hardness over time to more accurately reflect the physical processes  
344 controlling the incision depth. Detailed historical observations list the eruption  
345 duration as six to seven days in length (Sapper, 1925). The effusive phase of  
346 the 2015 eruption persisted for the same amount of time, but replaced the

347 majority of the lava within the first two days. Collectively, these observations  
348 allow us to place constraints on the rate of change of hardness (Fig. 9). Future  
349 work involves laboratory determination of the tensile strength and hardness of  
350 Momotombo lavas and cinders to refine these results.

## 351 4.2 Channel Growth

352 We calculate that the eroded volume is equal to roughly 2% of the total volume  
353 of the 1905 lava flow. Given the low eruptive temperature of basaltic andesites,  
354 it is unlikely that this material was fully assimilated into the flow. As the  
355 material heats and softens it is likely dragged downslope along the base of  
356 the flow for a short distance and then re-deposits, which creates a scalloped  
357 type signal for the measure of incision depth against elevation (Fig. 6). The  
358 thicknesses of subsequent lava flows will respond to this subtle topographic  
359 variability (i.e., more lava will be deposited in the troughs, less on the crest),  
360 which we find to be true for the 2015 flow (Fig. 6). We find no physical evidence  
361 of entrained substrate fragments at the base of the 1905 flow. Although other  
362 authors have noted geochemical evidence for assimilation of the substrate into  
363 the flow (e.g., Williams et al., 2004), geochemical similarities between recent  
364 Momotombo eruptive products make this an unlikely scenario for Momotombo.  
365 We also note a strong correlation between incision and lack of developed levees  
366 in the 2012 TDX DEM, which suggests that erosion began early on during the  
367 eruption (Fig. 7, conceptualized in Fig. S2F). This implies that levee bounded  
368 incised channels are not thermo-mechanically eroded, which is an important  
369 consideration for studies of incised channels on other planetary bodies.

370 Similar channels observed on the Moon exhibit nested rille structures (Hur-  
371 witz et al., 2013). These features might indicate that the tendency for extant  
372 channels to become catchments for later lava flows at Momotombo also exists

373 for lower sloped, larger volume lava flows on the Moon. If this pattern of re-  
374 peated occupation of rilles on the Moon was common then in addition to nested  
375 rilles, partially-infilled shallow rilles should exist, similar to the current chan-  
376 nel at Momotombo, which has now been partially filled with the most recently  
377 erupted lava. While it is certainly possible that nested rilles might form from  
378 a single effusive eruption, we note that the channels on Momotombo have sim-  
379 ple, single grooved, shapes. This could be in part due to the small volume of  
380 the flow and its short eruption timeline, or because of the high slope compared  
381 to rille-present lunar environments, which increases the efficacy of mechanical  
382 erosion (Williams et al 1998). However, our findings that substrate hardness  
383 plays a key role in thermomechanical erosion and that this hardness significantly  
384 decreases around the glass transition indicates that thermomechanical erosion  
385 by lavas through low sloping, unconsolidated regolith might play a larger role  
386 than previously hypothesized.

### 387 **4.3 Morphologic Implications**

388 The depth of a thermally eroded channel is limited by the efficiency of heat  
389 transfer across the boundary between the lava flow and the substrate, the rate  
390 of heat transfer in the subsurface, and the duration of an eruption (Kerr, 2001);  
391 when combined with morphologic studies of emplacement conditions (especially  
392 time), a constraint can be placed on the maximum depth of erosion. Channels  
393 whose incision depth exceeds this threshold indicate a preferential hardness  
394 ratio of the substrate to the flow (i.e., it is softer than the overriding flow)  
395 and can therefore be used to determine the presence of pyroclastic rocks and  
396 other easily eroded terrain (e.g., unconsolidated regolith and alluvial deposits)  
397 on planetary surfaces that can only be observed remotely. Large flows on the  
398 Moon, in particular, may be worth revisiting in light of these findings (Hurwitz



399 et al., 2013). Additionally, this suggests that the rate and depth of heat transfer  
400 for areas susceptible to incision may present a higher than normal hazard for  
401 buried infrastructure (Tsang et al., 2019).

402 A 1528 drawing of Momotombo, Infierno de mamea by Oviedo, shows a sim-  
403 ilar channel on the volcano’s west side. A channel on the northern flank (likely  
404 emplaced during an eruption in the second half of the 1800’s (Sapper, 1925))  
405 is also incised into the cone, and has been infilled by cinders from subsequent  
406 eruptions, which suggests the processes of slope incision and subsequent infill  
407 occurs with relative frequency on Momotombo. The preferential diversion of  
408 lava flows into incised channels for future events suggest that lava flow hazards  
409 on some steep-sided volcanoes are influenced by the creation, infill, and eventual  
410 abandonment of these structures. The channel may limit the lava flow hazard  
411 for the western flank if the next eruption is similar in size. Understanding the  
412 evolution of these features has important implications for lava flow hazards and  
413 growth patterns and erosion of composite volcanoes. Similar features can be  
414 found on Sierra Negra (Galápagos). Syn-eruptive erosion suggests a strength  
415 differential in the materials that construct some volcanic cones, which can in-  
416 dicate increased susceptibility to internal structural instabilities. Incision into  
417 cinder cones via flowing lava likely plays a major role in their destruction, which  
418 in turn impacts subsequent flow inundation patterns.

## 419 **5 Conclusions**

420 We use satellite (TDX) and terrestrial radar (TRI) DEMs to obtain a detailed  
421 record of recent changes to the edifice of Momotombo Volcano from 2012–2017,  
422 during which a VEI-2 eruption occurred. We describe a unique lava channel  
423 that incised 25–35 m into the northeast sector of the volcano near the summit  
424 and transitions into a constructional channel roughly halfway down the edifice.

425 We assert that this feature formed erosively during the emplacement of a lava  
426 flow in 1905 and note a direct correlation between a lack of levees and incision  
427 depth. Thermal erosion alone was unable to account for the full depth of incision  
428 and we suggest that thermo-mechanical erosion is the likely cause. We examine  
429 inputs from mechanical models of erosion and determine that, based on the  
430 relationship between material hardness and shear strength, these models should  
431 be re-classified as thermo-mechanical. We propose that the transfer of heat  
432 into the substrate decreases the hardness of the material, which encourages it  
433 to flow more readily and excavate, in agreement with modeling approaches by  
434 Huppert et al. (1984) and Williams et al. (1998). We establish that the critical  
435 temperature at which this occurs is lower than previously thought, likely at the  
436 glass transition temperature (1013K), instead of the liquidus of a given lava. We  
437 calculate the total eroded volume to be  $4 \times 10^5 \text{ m}^3$  and determine that erosion  
438 is likely to occur when the hardness of the substrate is less than  $4 \times 10^6 \text{ Pa}$ .  
439 Deeply incised channels control the distribution of future flows and can also  
440 be used to infer the material properties of the substrate into which they are  
441 excavated.

## 442 **Acknowledgments**

443 Funding for field work was provided by NSF EAR 1620977: Geochemical and  
444 Geophysical Observations of the 2015 Eruption of Volcan Momotombo, Nicaragua,  
445 awarded to PL, CC, and others. Deployment of the TRI was partially funded by  
446 NSF RAPID grant EAR 1546924 to THD and SC. Field support was provided  
447 by many staff members at INETER. We thank the German Aerospace Center  
448 (DLR) for providing TanDEM-X SAR data. Equipment logistics were eased by  
449 the efforts of Denis Voytenko, Milton Ordonez, and Anderson at the Servicio  
450 Geológico Colombiano. The manuscript's clarity was improved by feedback from  
451 Jen Bright and Christopher Sant. Pam Wayne and Jose Rincon were crucial  
452 in facilitating this feedback. We thank Heather Handley (editor) and reviewers  
453 Jamie Farquharson and David Williams for their quick and thoughtful feedback.

454

## 455 **References**

- 456 Baker, V. R., Komatsu, G., Parker, T. J., Gulick, V. C., Kargel, J. S., and  
457 Lewis, J. S. (1992). Channels and valleys on Venus: Preliminary analysis of  
458 Magellan data. *Journal of Geophysical Research. Planets*, 97(E8):13421.
- 459 Beresford, S., Cas, R., Lahaye, Y., and Jane, M. (2002). Facies architecture of an  
460 archean komatiite-hosted ni-sulphide ore deposit, victor, kambalda, western  
461 australia: implications for komatiite lava emplacement. *Journal of Volcanol-*  
462 *ogy and Geothermal Research*, 118(1):57 – 75.
- 463 Bilotta, G., Cappello, A. and Herault, A., and Del Negro, C. (2019). Influ-  
464 ence of topographic data uncertainties and model resolution on the numerical  
465 simulation of lava flows. *Environmental Modelling and Software*, 112:1–15.
- 466 Caduff, R., Schlunegger, F., Kos, A., and Wiesmann, A. (2015). A review of ter-  
467 restrial radar interferometry for measuring surface change in the geosciences.  
468 *Earth Surface Processes and Landforms*, (2):208.
- 469 Carr, M. (1974). The role of lava erosion in the formation of lunar rilles and  
470 martian channels. *Icarus*, 22(1):1 – 23.
- 471 Carr, M. J. and Pontier, N. K. (1981). Research paper: Evolution of a young  
472 parasitic cone towards a mature central vent; Izalco and Santa Ana volcanoes  
473 in El Salvador, Central America. *Journal of Volcanology and Geothermal*  
474 *Research*, 11:277 – 292.
- 475 Connor, C., Lichtner, P., Conway, F., Hill, B., Ovsyannikov, A., Federchenko,  
476 I., Doubik, Y., Shapar, V., and Taran, Y. A. (1997). Cooling of an igneous  
477 dike 20 yr after intrusion. *Geology*, (8):711.

478 Courtland, L. M., Kruse, S. E., Connor, C. B., Connor, L. J., Savov, I. P.,  
479 and Martin, K. T. (2012). Gpr investigation of tephra fallout, cerro negro  
480 volcano, nicaragua: a method for constraining parameters used in tephra  
481 sedimentation models. *Bulletin of Volcanology*, (6):1409.

482 Deng, F., Rodgers, M., Xie, S., Dixon, T., Charbonnier, S., Gallant, E., Lopez-  
483 Velez, C., Ordonez, M., Malservisi, R., Voss, N., and Richardson, J. (2019).  
484 High-resolution dem generation from spaceborne and terrestrial remote sens-  
485 ing data for improved volcano hazard assessment — a case study at nevado  
486 del ruiz, colombia. *Remote Sensing of Environment*, 233:1113–1148.

487 Dietterich, H., Lev, E., Chen, J., Richardson, J., and Cashman, K. (2017).  
488 Benchmarking computational fluid dynamics models of lava flow simulation  
489 for hazard assessment, forecasting, and risk management. *Journal of Applied*  
490 *Volcanology*, 6(1):1.

491 Dietterich, H. R. and Cashman, K. V. (2014). Channel networks within lava  
492 flows: Formation, evolution, and implications for flow behavior. *Journal of*  
493 *Geophysical Research. Earth Surface*, 119(8):1704.

494 Dixon, T. H., Voytenko, D., Lembke, C., Peña, S., Howat, I., Gourmelen, N.,  
495 Werner, C., and Oddsson, B. (2012). Emerging technology monitors ice-sea  
496 interface at outlet glaciers. *Eos (0096-3941)*, 93(48):497.

497 Dundas, C. M. and Keszthelyi, L. P. (2014). Emplacement and erosive effects  
498 of lava in south Kasei Valles, Mars. *Journal of Volcanology and Geothermal*  
499 *Research*, 282:92 – 102.

500 Fagents, S. A. and Greeley, R. (2001). Factors influencing lava-substrate heat  
501 transfer and implications for thermomechanical erosion. *Bulletin of Volcanol-*  
502 *ogy*, (8):519.

503 Farquharson, J. I., Heap, M. J., and Baud, P. (2016). Strain-induced perme-  
504 ability increase in volcanic rock. *Geophysical Research Letters*, 43(22):11,603.

505 Fox, M. (2019). A linear inverse method to reconstruct paleo-topography. *Ge-*  
506 *omorphology*, 337:151 – 164.

507 Germa, A., Lahitte, P., and Quidelleur, X. (2015). Construction and destruction  
508 of Mont Pelée volcano: Volumes and rates constrained from a geomorpho-  
509 logical model of evolution. *Journal of Geophysical Research. Earth Surface*,  
510 120(7):1206.

511 Giordano, D., Nichols, A. R., and Dingwell, D. B. (2005). Glass transition  
512 temperatures of natural hydrous melts: a relationship with shear viscosity  
513 and implications for the welding process. *JOURNAL OF VOLCANOLOGY*  
514 *AND GEOTHERMAL RESEARCH*, (1-2):105.

515 Global Volcanism Program (2017). Report on Momotombo (Nicaragua). In Ven-  
516 zke, E., editor, *Bulletin of the Global Volcanism Network*, volume 42:1, Smith-  
517 sonian Institution. <https://doi.org/10.5479/si.GVP.BGVN201701-344090>.

518 Gottsmann, J. and Dingwell, D. B. (2002). The thermal history of a spatter-fed  
519 lava flow: the 8-ka pantellerite flow of mayor island, new zealand. *Bulletin of*  
520 *Volcanology*, 64(6):410–422.

521 Greeley, R., Fagents, S. A., Scott Harris, R., Kadel, S. D., Williams, D. A.,  
522 and Guest, J. E. (1998). Erosion by flowing lava: Field evidence. *Journal of*  
523 *Geophysical Research*, (B11):27.

- 524 Head, J. W. and Wilson, L. (2017). Generation, ascent and eruption of magma  
525 on the Moon: New insights into source depths, magma supply, intrusions  
526 and effusive/explosive eruptions (Part 2: Predicted emplacement processes  
527 and observations). *Icarus*, 283(Lunar Reconnaissance Orbiter - Part II):176  
528 – 223.
- 529 Hill, B. E., Connor, C. B., Jarzempa, M. S., La Femina, P. C., Navarro, M., and  
530 Strauch, W. (1998). 1995 eruptions of cerro negro volcano, nicaragua, and  
531 risk assessment for future eruptions. *Geological Society of America Bulletin*,  
532 (10):1231.
- 533 Hobden, B. J., Houghton, B. F., and Nairn, I. A. (2002). Growth of a young,  
534 frequently active composite cone: Ngauruhoe volcano, New Zealand. *Bulletin*  
535 *of Volcanology*, (6):392.
- 536 Hulme, G. (1973). Turbulent lava flow and the formation of lunar sinuous rilles.  
537 *Modern Geology*, 4:107–117.
- 538 Huppert, H., Sparks, R., and Turner, J. (1984). Emplacement and cooling of  
539 komatiite lavas. *Nature*, 309:19 – 22.
- 540 Hurwitz, D. M., Fassett, C. I., Head, J. W., and Wilson, L. (2010). Formation  
541 of an eroded lava channel within an Elysium Planitia impact crater: Dis-  
542 tinguishing between a mechanical and thermal origin. *Icarus*, 210(2):626 –  
543 634.
- 544 Hurwitz, D. M., Head, J. W., and Hiesinger, H. (2013). Lunar sinuous rilles:  
545 Distribution, characteristics, and implications for their origin. *Planetary and*  
546 *Space Science*, 79-80:1–38.

547 Intercontinental Railway Commission (1898). A Condensed Report of the Trans-  
548 actions of the Commission and of the Surverys and Explorations of its Engi-  
549 neers in Central and South America.

550 Jaeger, J. C., Cook, N. G. W., and Zimmerman, R. W. (2007). *Fundamentals*  
551 *of rock mechanics. [electronic resource]*. Blackwell Pub.

552 Kauahikaua, J., Cashman, K. V., Mattox, T. N., Heliker, C. C., Hon, K. A.,  
553 Mangan, M. T., and Thornber, C. R. (1998). Observations on basaltic lava  
554 streams in tubes from Kilauea Volcano, island of Hawai'i. *Journal of Geo-*  
555 *physical Research. Solid Earth*, 103(B11):27303.

556 Kerr, R. C. (2001). Thermal erosion by laminar lava flows. *Journal of Geophys-*  
557 *ical Research*, (11):26.

558 Kerr, R. C., Griffiths, R. W., and Cashman, K. V. (2006). Formation of chan-  
559 nelized lava flows on an unconfined slope. *Journal of Geophysical Research:*  
560 *Solid Earth (1978–2012)*, 111(B10).

561 Kilburn, C. R. J. and Lopes, R. M. C. (1988). The growth of AA lava flow  
562 fields on Mount Etna, Sicily. *Journal of Geophysical Research: Solid Earth*,  
563 93(B12):14759–14772.

564 Kirainov, V., Melekestev, I., Ovsyannikov, A., and Andreev, V. (1988). Re-  
565 construction of the eruptive activity of momotombo volcano (nicaragua) to  
566 assess volcanic hazards. pages 495 – 498.

567 Krieger, G., Moreira, A., Fiedler, H., Hajnsek, I., Werner, M., Younis, M.,  
568 and Zink, M. (2007). TanDEM-X: A Satellite Formation for High-Resolution  
569 SAR Interferometry. *IEEE Transactions on Geoscience and Remote Sensing*,  
570 (11):3317.



- 571 Miller, A. A. (1963). Free volume and viscosity of liquids: Effects of temperature.  
572 *The Journal of Physical Chemistry*, 67(5):1031–1035.
- 573 Patrick, M. R., Dehn, J., and Dean, K. (2004). Numerical modeling of lava  
574 flow cooling applied to the 1997 okmok eruption: Approach and analysis (doi  
575 10.1029/2003jb002537). *JOURNAL OF GEOPHYSICAL RESEARCH -ALL*  
576 *SERIES-*, (3):B03202.
- 577 Peterson, D. W., Holcomb, R. T., Tilling, R. I., and Christiansen, R. L. (1994).  
578 Development of lava tubes in the light of observations at Mauna Ulu, Kilauea  
579 Volcano, Hawaii. *Bulletin of Volcanology*, (5):343.
- 580 Richardson, P. and Karlstrom, L. (2019). The multi-scale influence of topogra-  
581 phy on lava flow morphology. *Bulletin of Volcanology*, (4):1.
- 582 Robl, J., Stüwe, K., and Hergarten, S. (2008). Channel profiles around hi-  
583 malayan river anticlines: Constraints on their formation from digital elevation  
584 model analysis. *Tectonics*, 27(3).
- 585 Sapper, K. (1916). Die mittelamerikanische Landschaft. *Geographische*  
586 *Zeitschrift*, 8(9):489.
- 587 Sapper, K. (1925). *Los volcanes de la America Central*. Halle: Verlag von Max  
588 Niemeyer.
- 589 Schenk, P. M. and Williams, D. A. (2004). A potential thermal erosion lava  
590 channel on Io. *Geophysical Research Letters*, 31(23).
- 591 Siewert, J. and Ferlito, C. (2008). Mechanical erosion by flowing lava. *Contem-*  
592 *porary Physics*, (1):43.
- 593 Sklar, L. and Dietrich, W. E. (1998). River Longitudinal Profiles and Bedrock  
594 Incision Models: Stream Power and the Influence of Sediment Supply. *Geo-*  
595 *physical Monograph - American Geophysical Union*, page 237.

596 Staude, S., Barnes, S. J., and Le Vaillant, M. (2017). Thermomechanical ero-  
597 sion of ore-hosting embayments beneath komatiite lava channels: Textural  
598 evidence from kambalda, western australia. *Ore Geology Reviews*, 90:446 –  
599 464.

600 Strozzi, T., Werner, C., Wiesmann, A., and Wegmuller, U. (2012). Topogra-  
601 phy Mapping With a Portable Real-Aperture Radar Interferometer. *IEEE*  
602 *Geoscience and Remote Sensing Letters*, (2):277.

603 Tsang, S. W. R., Lindsay, J. M., Coco, G., Wysocki, R., Lerner, G. A., Rader,  
604 E., and Turner, G. M. (2019). The heating of substrates beneath basaltic lava  
605 flows. *Bulletin of Volcanology*, (11):1.

606 Turcotte, D. L., Turcotte, D. L., and Schubert, G. (2002). *Geodynamics*. Cam-  
607 bridge ; New York : Cambridge University Press.

608 Vincent, F. (1890). In and out of Central America.

609 Voytenko, D., Dixon, T. H., Luther, M. E., Lembke, C., Howat, I. M., and de la  
610 Peña, S. (2015). Observations of inertial currents in a lagoon in southeastern  
611 Iceland using terrestrial radar interferometry and automated iceberg tracking.  
612 *Computers and Geosciences*, 82:23 – 30.

613 Werner, C., Wegmüller, U., Strozzi, T., and Wiesmann, A. (2000). Gamma sar  
614 and interferometric processing software. volume 1620, page p. 1620.

615 Williams, D., Kadel, S., Greeley, R., Leshner, C., and Clynne, M. (2004). Erosion  
616 by flowing lava: geochemical evidence in the Cave Basalt, Mount St. Helens,  
617 Washington. *Bulletin of Volcanology*, (2).

618 Williams, D. A., Kerr, R. C., and Leshner, C. M. (1998). Emplacement and  
619 erosion by Archean komatiite lava flows at Kambalda: Revisited. *Journal of*  
620 *Geophysical Research*, (B11):27.

- 621 Williams-Jones, G., Williams-Jones, A. E., and Stix, J. (1998). The nature  
622 and origin of Venesian canali. *Journal of Geophysical Research. Planets*,  
623 103(E4):8545.
- 624 Wilson, L. and Head, J. W. (2017). Generation, ascent and eruption of magma  
625 on the Moon: New insights into source depths, magma supply, intrusions and  
626 effusive/explosive eruptions (Part 1: Theory). *Icarus*, 283(Lunar Reconnaissance  
627 Orbiter - Part II):146 – 175.
- 628 Wooster, M. J., Wright, R., Blake, S., and Rothery, D. A. (1997). Cooling  
629 mechanisms and an approximate thermal budget for the 1991-1993 Mount  
630 Etna lava flow. *Geophysical Research Letters*, (24):3277.
- 631 Xie, S., Dixon, T. H., Voytenko, D., Fanghui, D., and Holland, D. M. (2018).  
632 Grounding line migration through the calving season at Jakobshavn Is-  
633 bræ, Greenland, observed with terrestrial radar interferometry. *Cryosphere*,  
634 12(4):1387 – 1400.
- 635 Zum Gahr, K.-H. (1998). Wear by hard particles. *Tribology International*,  
636 (10):587.

Table 1: Momotombo erosion model variables, input parameters, and sources

variable	meaning	value (units)	source
N/A	volume of 1905 lava flow	$2 \times 10^7$ (m <sup>3</sup> )	this study (DEM analysis)
N/A	volume of eroded channel	$4 \times 10^5$ (m <sup>3</sup> )	this study (DEM analysis)
$\rho$	density of 1905 lava	2600 (kg m <sup>-1</sup> )	this study
$\rho_s$	density of cinders	1000 (kg m <sup>-1</sup> )	this study
$c_l$	specific heat capacity for lava	1400 (J kg <sup>-1</sup> )	this study (MELTS)
$T_l$	lava temperature	1325 (K)	this study (FLIR)
$T_s$	initial substrate temperature	300 (K)	this study (FLIR)
$\phi$	mass fraction crystallization	50 %	this study (sample)
$F$	latent heat of fusion	$2.5 \times 10^5$ (J kg <sup>-1</sup> )	analogous flow, Siewert and Ferlito (2008)
$y$	depth into substrate	see Fig. 8	this study
$t$	eruption duration	2–5 days	Sapper (1916)
$\kappa$	thermal diffusivity	$2.5 \times 10^{-7}$ m <sup>2</sup> s <sup>-1</sup>	this study
$\eta T$	similarity variable	0.3	this study
$k_T$	thermal conductivity	0.2 (W m <sup>-1</sup> K <sup>-1</sup> )	Connor et al., 1997
$c$	specific heat capacity for cinders	800 (J kg <sup>-1</sup> K <sup>-1</sup> )	this study (MELTS)
$e, frc$	complementary error function	0.4286	this study
$\theta_r$	dimensionless similarity variable	0.7	this study
$T_e$	temperature for erosion initiation	1013 K	Giordano et al. (2005)
$k$	wear coefficient	0.01–0.001	analogous flow, Siewert and Ferlito (2008)
$h$	lava flow thickness (in channel)	3 m	this study (2015 flow)
$v$	average lava flow velocity	0.25–1.75 (m s <sup>-1</sup> )	this study
$\theta$	slope	locally variable: 5–35°	this study (DEM analysis)
$d_{channel}$	depth of erosion	0–30 (m)	this study (DEM analysis)
<b>model output</b>	<b>meaning</b>	<b>value (units)</b>	<b>source</b>
$E_{thermal}$	total thermal energy of 1905 flow	$7 \times 10^{16}$ (J)	this study
$E_{eroded}$	thermal energy required to erode channel	$2 \times 10^{14}$ (J)	this study
$H$	substrate hardness	see Fig. 9B	this study

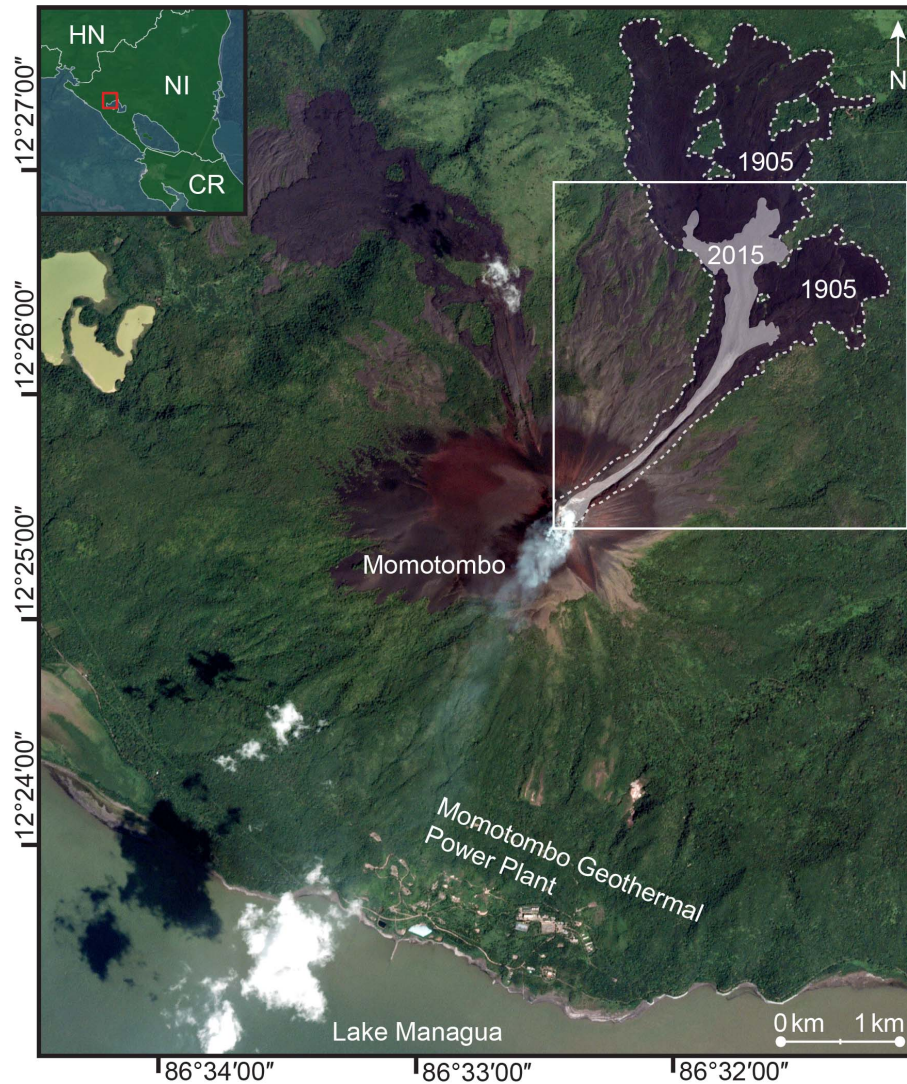


Figure 1: Momotombo area map. The most recent volcanism (a lava flow emitted during the 2015-2016 eruption) is noted by a light-grey overlay. The 1905 eruption is noted by a dotted line. The area shown in Fig. 4 is noted by the white box. Note the widely dispersed flows that underlie the 2015 and 1905 flows. Their distribution suggests that no incised channel existed at the time of their emplacement to direct flow paths. Background image from GoogleEarth.

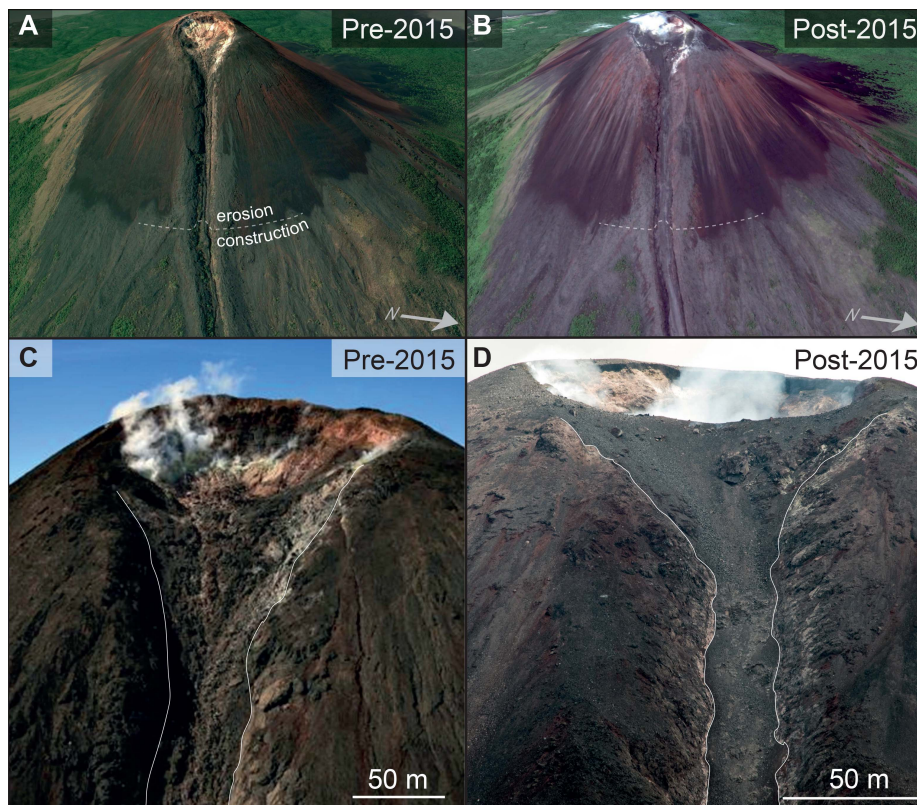


Figure 2: Pre and post 2015-2016 eruption images of the Momotombo channel and summit. A) A pre-eruption image of the channel, where the dashed line shows the approximate transition between erosional and constructional behavior. B) Major changes in morphology can be seen in and around the summit crater, where the 2015 lava flow first filled and was then partially excavated during subsequent explosions in 2016. The pre-existing floor of the channel has been paved over by a lava flow and appears less 'rough' than the pre-eruption channel floor. Images A and B from Google Earth. C) The summit crater prior to the 2015-2016 eruption, with white lines bounding the channel. Textures within the channel indicate downslope flow. Image from INETER. D) The summit area on 6 April, 2016. Several hundred small explosions have partially excavated a small dome from December, 2015. Blocks have been deposited atop the recent lava flow and a fine, grey layer of ash from repeated pyroclastic density currents coats the channel.

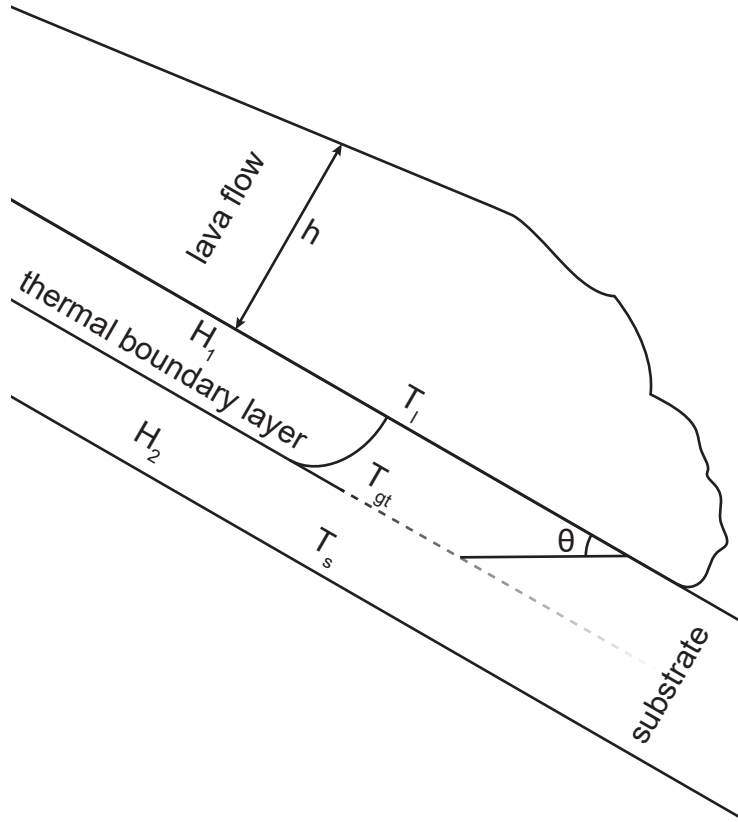


Figure 3: Simplified model of thermal boundary formation. The energy required to melt a pyroclast-rich substrate is less than that of a lava flow because of a lower density; we can therefore substitute the peak glass transition temperature (1013 K) as the minimum temperature required to initiate melting for such substrates (Giordano et al., 2005). The formation of the thermal boundary layer shows the transition between the temperature of the lava ( $T_l$ ) and the substrate ( $T_s$ ). This layer defines the boundary between a thermally softened substrate ( $H_1$ ) and the unaffected substrate ( $H_2$ ). The height of the lava flow is noted by  $h$  and the slope of the edifice by  $\theta$ .

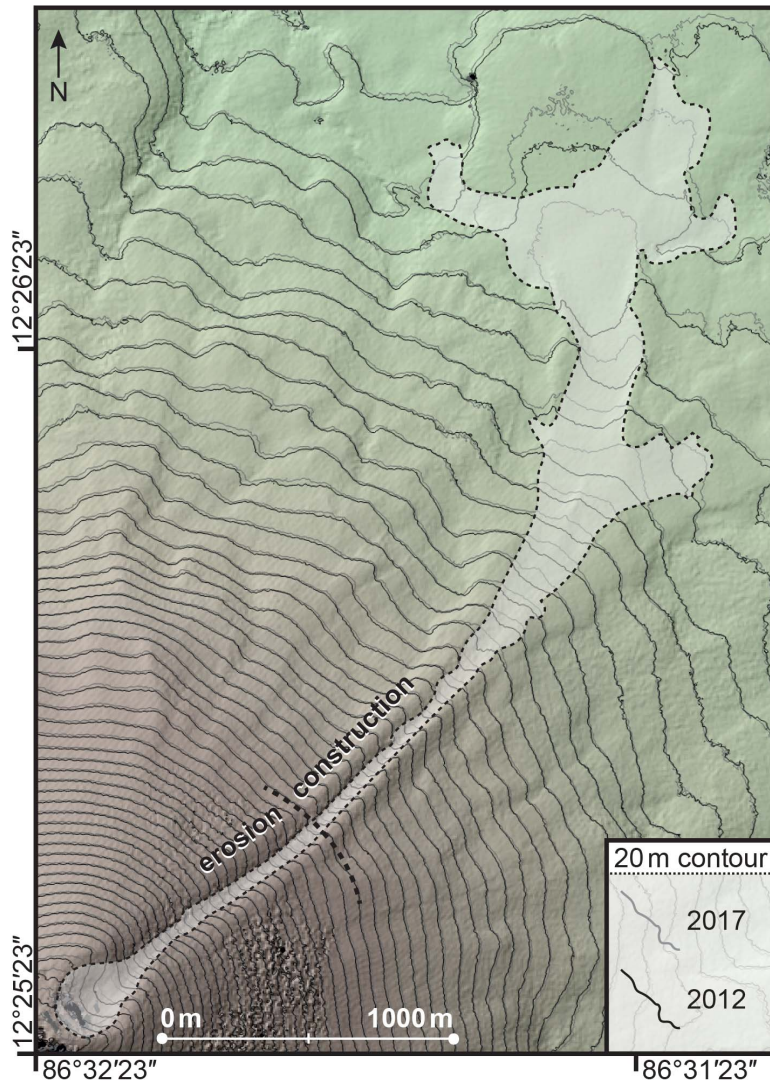


Figure 4: Elevation contour difference measured from the 2012 and 2017 TDX DEMs. Elevation contours at 20 m intervals were mapped from the TDX datasets; the grey contours represent the 2017 elevations (post 2015-2016 eruption), and the black represent the 2012 elevations. Slight contour variations exist in areas not impacted by the 2015-2016 eruption because of the different look angles of the TDX data pairs and georeferencing uncertainties. The white infill shows the area covered by the 2015 lava flow and the thick dashed line shows the approximate area of transition between erosion and construction (~650 m).



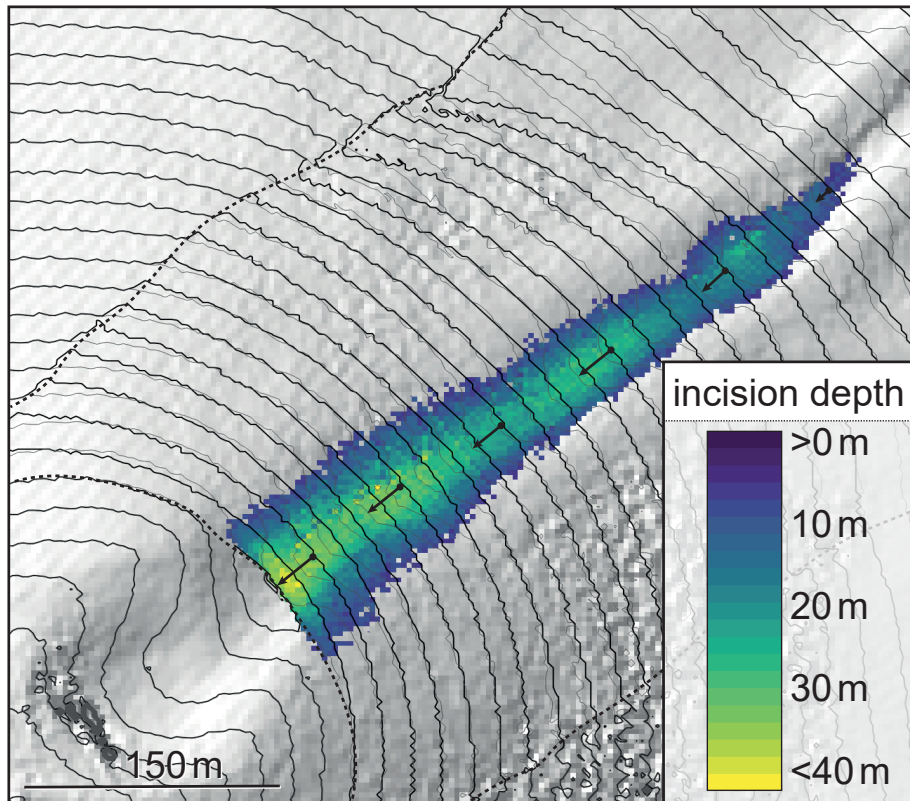


Figure 5: Elliptical contour fit incision depth process (from 2012 DEM). The original elevation contours at 20 m intervals are noted in grey, the modeled fit in black. Incision depths, with arrows that indicate the horizontal distance between the modeled paleotopography and the current point of corresponding incision. Incision is deepest at the summit and decreases downslope until  $\sim 650$  m, where the channel transitions into a constructional features.

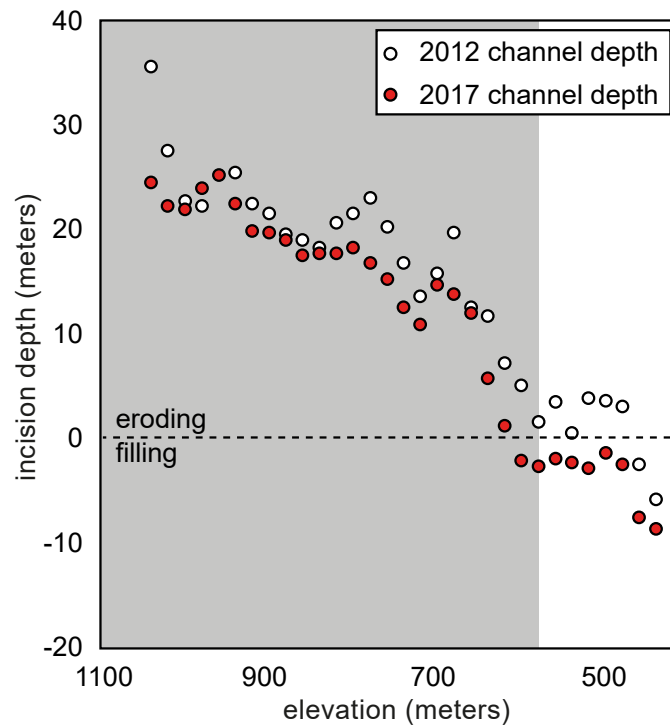


Figure 6: Calculated channel depths at 20-m elevation intervals before and after the eruption, using the elliptical fit method described in Figure 5. Calculated channel depths and slopes at 20-m elevation intervals before and after the eruption. White and red dots are channel depths of the pre- and post-eruption channel, respectively. The difference of the two DEMs gives us the thickness of the 2015 lava flow. The grey shading indicates the elevation range where erosion dominates ( $>650$  m).

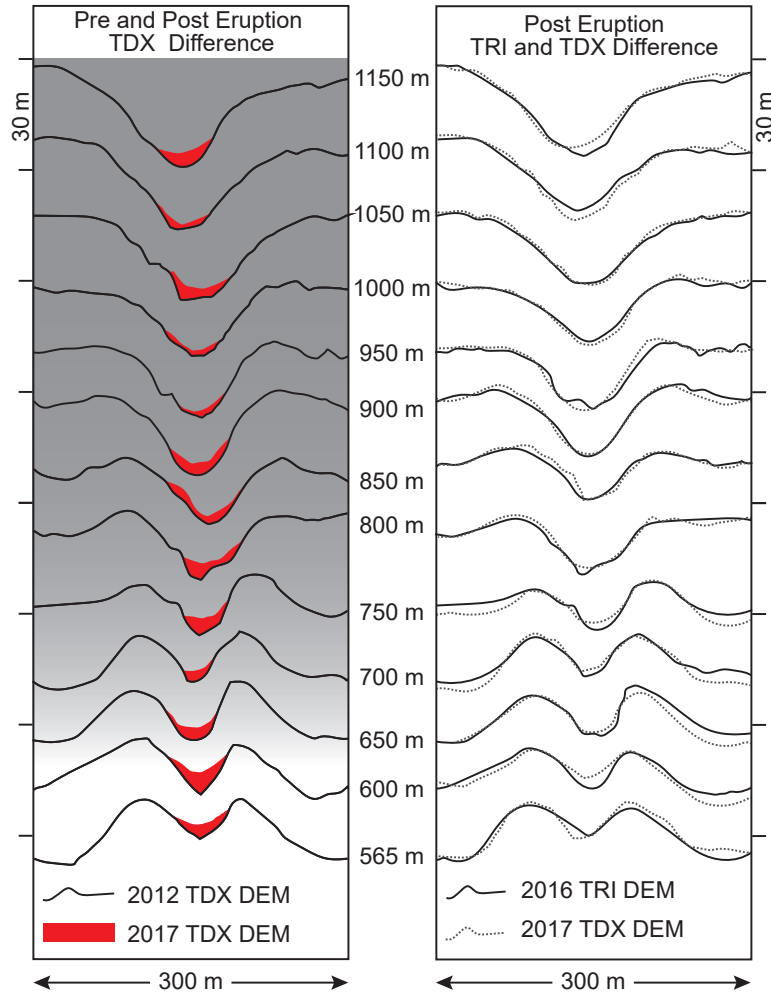


Figure 7: Momotombo lava channel profiles. The left figure shows channel profiles from the 2012 TDX DEM and an overlay of the lava flow from 2015. The 2012 profile is noted by the solid black line, with the 2015 lava flow (imaged by the 2017 TDX acquisition) by the red polygon. The grey shading illustrates the transition of channel into a constructional feature at  $\sim 650$  m. The profiles have been visually adjusted to match up topography in order to account for the  $21^\circ$  difference in acquisition angles. The right figure shows the difference between the 2016 TRI DEM and the 2017 TDX DEM. Comparison of the post-eruption profiles estimates the relative noise of the DEMs.

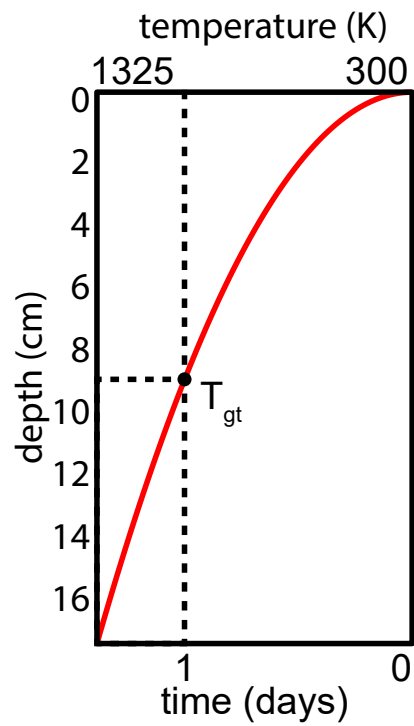


Figure 8: Substrate thermal boundary layer. At one day, we calculate the thermal boundary layer for a flow on Momotombo to grow to 8.8 cm. Thermal erosion rates in Hawaiian tubes and channels can reach  $\sim 10$  cm per day (Kauahikaua et al., 1998); given the lower temperature of lavas erupted on Momotombo, it is reasonable to assume a slower rate of thermal boundary growth.

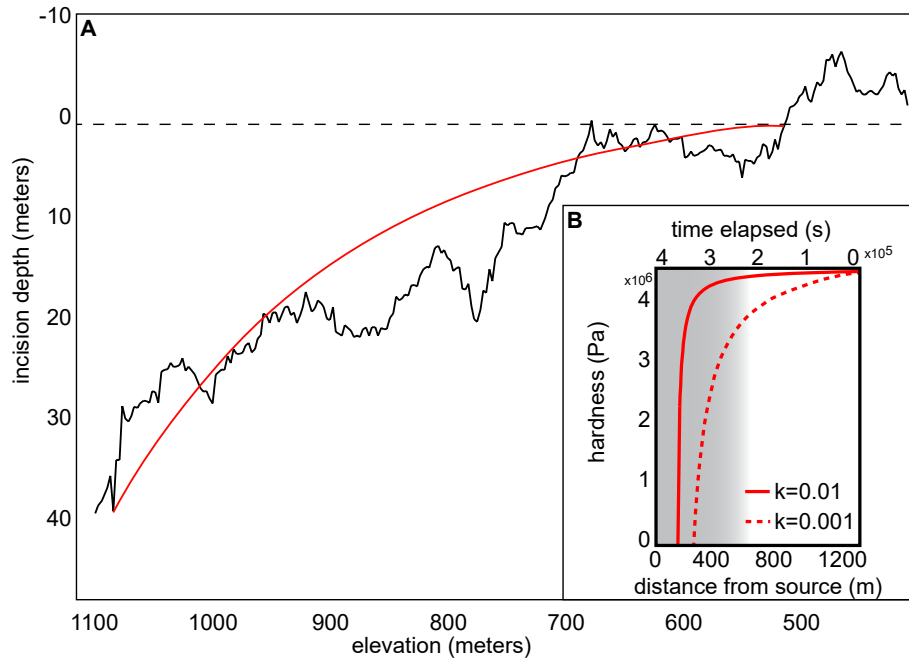


Figure 9: Incision depth fit models. A: Depth is used as a proxy for time in order to constrain the hardness ( $H$ ) of the eroded substrate. The red line indicates the exponential fit to the eroded depth as a function of elevation. The dotted line indicates the the transition from erosion (below) to construction (above). B: Substrate hardness as a function of time and distance. Time elapsed is the total time the substrate is in contact with flowing lava. The grey shading illustrates the transition of channel into a constructional feature at  $\sim 650$  m. We model the change of  $H$  as a function of time and distance for different values of the wear coefficient,  $k=0.01$ , as the solid red line and  $k=0.001$  as the dotted red line.

637 **Supplemental Material**

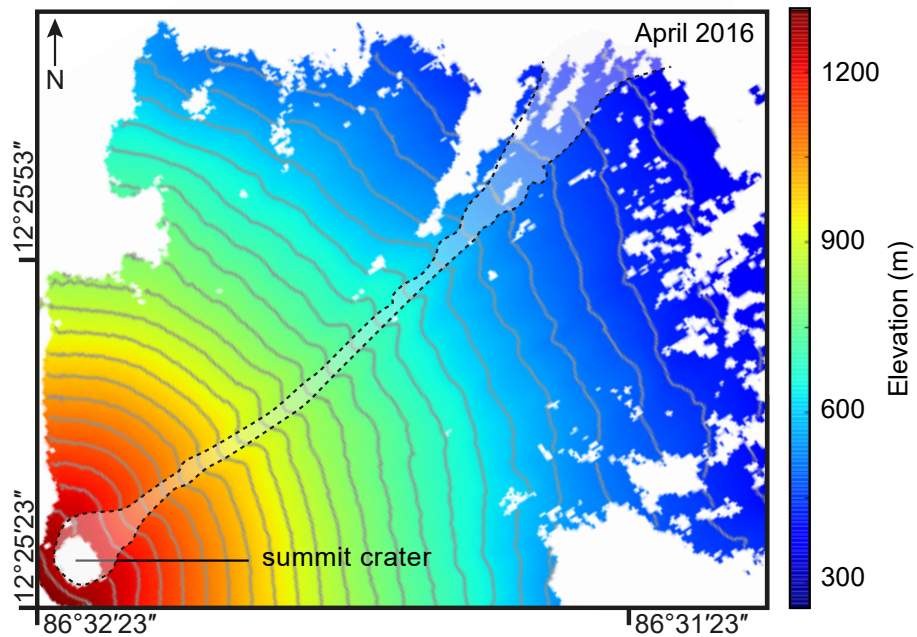


Figure 10: 2016 Terrestrial Radar DEM. The white infill and black dashed line shows the area covered by the 2015 lava flow. The absence of signal near the summit shows the  $120 \times 100$  m crater, which was excavated by several hundred small explosions between December 2015 and April 2016. The grey lines indicate 20 m contour intervals.

638 **Paleotopography Modeling Code**

639 The MatLab code and associated functions used to model the paleotopogra-  
640 phy of the erosive channel and determine excavation depths is available at  
641 [https://github.com/elisabeth-gallant/Paleotopography\\_Reconstruction](https://github.com/elisabeth-gallant/Paleotopography_Reconstruction).

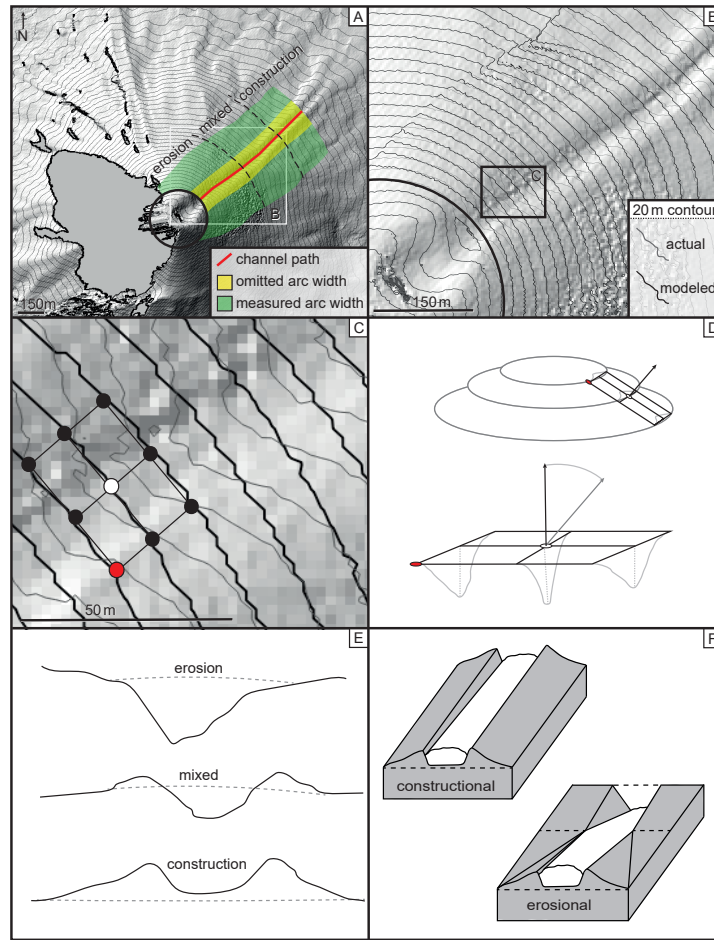


Figure 11: Elliptical contour fit incision depth process (from 2012 DEM). A: The center of the channel is noted in red, area used to calculate the best fit contours in green, and the area omitted from the contour calculation in yellow. The dashed line shows the approximate boundary between erosional, mixed, and constructional regimes (described in profile in panel F). B: The original elevation contours at 20 m intervals are noted in grey, the modeled fit in black. C: The orientation of vectors normal to the edifice are calculated using a  $9 \times 9$  matrix. The distance between sampling points is enlarged to illustrate the concept. D: The matrix is transposed so that the only magnitude of the vector is in the z-direction. The elevation value is returned as a weighted-average of the constituent points (with distance from the center as the weighting criteria). E: The simplified profiles for erosional, mixed, and constructional regimes, with a dashed line denoting the paleosurface. F: Constructional (left) vs erosional (right) behaviour in lava channels on an incline. We note the change in slope associated with the original orientation of the incline and the eroded portion. The dashed line notes the paleotopography surface. Additionally, levees are absent from the incised section of the channel. Profiles of these different regimes are presented in Figure 8.

## 642 **Circular Contour Fit**

643 Channel incision depths were measured by interpolating best-fit 20-m interval  
644 contour lines to the overall shape of the edifice using the 2012 TDX DEM. Each  
645 interpolated contour line was calculated by fitting the original contour line with  
646 an arc using least-squares. The section proximal to the channel was not included  
647 in the fitting process because of its wide deviation from the overall shape of  
648 the cone. Depth at each sampled elevation was measured by determining the  
649 minimum distance between the interpolated contour line and the deepest point  
650 of the channel, measured normal to the slope of the edifice (Fig. 12b). All  
651 points on the contour line (not including the flow levees and the channel) were  
652 averaged to calculate the slope for each measured depth.

653 Results show the pre-2015 eruption channel extended down the northeast  
654 side of the edifice from the summit and continued for 2 km onto the surrounding  
655 plain (Fig. 13). A consistent width of  $\sim 30$  m was maintained throughout the  
656 channel's length, while incision depth varied from 35 m at the summit's rim and  
657 tapered off to 0 at  $\sim 700$  m elevation (Fig. 12a). The 1905 channel has been  
658 infilled with a lava flow from 2015 with a thickness  $< 3$  m (Fig. 13).



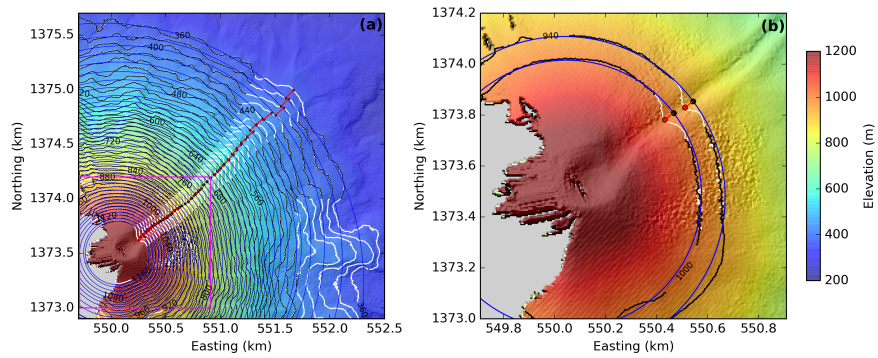


Figure 12: Channel depth calculation using the pre-eruption DEM as an example (a) 2012 DEM. Black and white lines are contours with 20 m interval. The blue circles are the best-fit arcs for each contour line. Contour lines in white were not used in the fitting processing because they include the topographic influence of the levees and channel, which greatly deviates from the circular fit. The red lines indicate the depth of the channel thalweg. (b) A zoomed in view of the fitting process. Red dots indicate the deepest points in the channel.

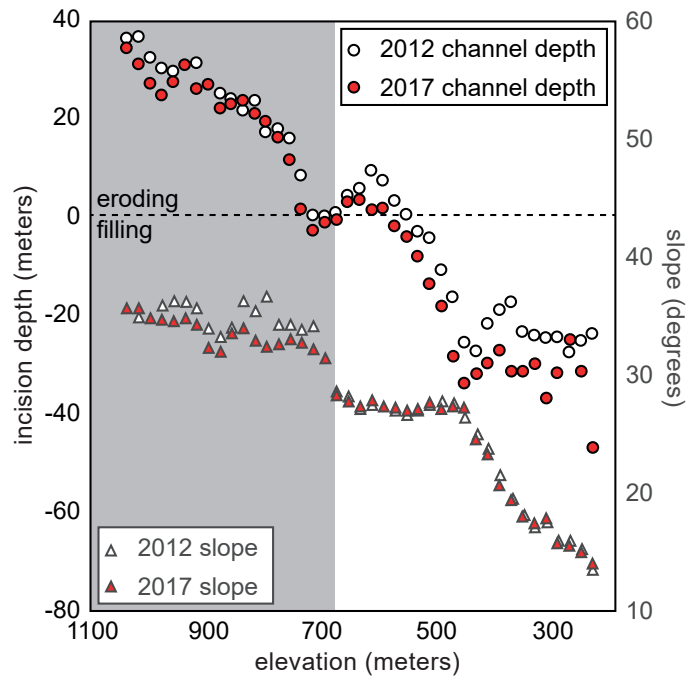


Figure 13: Calculated channel depths, slopes, and differences using the circular fit method. Calculated channel depths and slopes at 20-m elevation intervals before and after the eruption. White and red dots are channel depths of the pre- and post-eruption channel, respectively. The difference of the two DEMs gives us the thickness of the 2015 lava flow. White and red triangles are averaged slopes at 20-m elevation intervals of the pre- and post-eruption edifice.

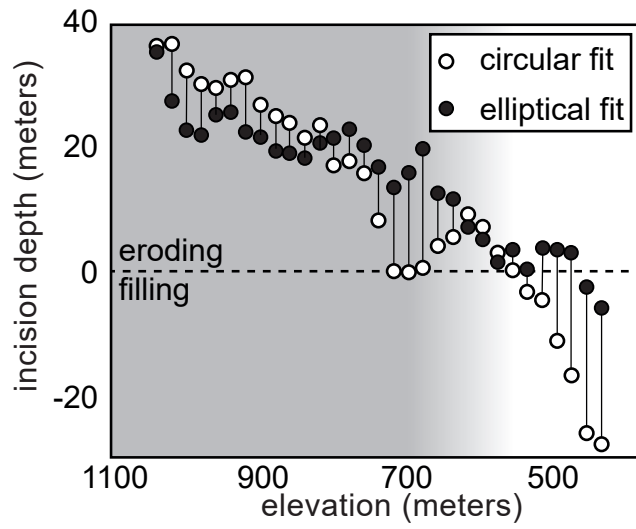


Figure 14: Comparison of the circular and elliptical method incision depths for the 2012 TDX DEM. The grey area indicates the transition between incision and construction, with a gradient to indicate the uncertainty between the two models as to where this occurs.